Spherical correlation as a similarity measure for 3D radiation patterns of musical instruments

Thibaut Carpentier, Aaron Einbond

16ème Congrès Français d'Acoustique
11-15 Avril 2022, Marseille

Spherical correlation as a similarity measure for 3D radiation patterns of musical instruments

T. Carpentier[a] et A. Einbond[b]

[a]STMS Lab – IRCAM, SU, CNRS, Ministère de la Culture – 1 place Igor Stravinsky, 75004 Paris, France
[b]City, University of London – Northampton Square, EC1V 0HB London, UK

This work is part of an artistic-research residency where composer Aaron Einbond seeks to apply audio descriptor analysis and corpus-based synthesis techniques to the spatial manipulation of instrumental radiation patterns for projection with a compact spherical loudspeaker array. Starting from a database of 3D directivity patterns of orchestral instruments, measured with spherical microphone arrays in anechoic conditions, we wish to derive spatial descriptors in order to classify the corpus. This paper investigates the use of spherical cross-correlation as a similarity measure between radiation patterns. Considering two directivity patterns f and g as bandlimited, square integrable functions on the 2-sphere, their correlation can be computed from their spherical harmonic spectra via a spatial inverse discrete Fourier transform. The magnitudes of these Fourier coefficients provide a rotation-invariant representation of the functions on the sphere. One can therefore search for the transformation matrix m, in the 3D rotation group $SO(3)$, which maximizes the cross-correlation, i.e. which offers the optimal spherical shape matching between f and g. The mathematical foundations of these tools are well established in the literature; however, their practical use in the field of acoustics remains limited and challenging. In this study, we apply these techniques to both simulated and measured radiation data, attempting to answer a number of practical questions : How does the similarity measure behave when f and g are not rotated cousins ? How can we adapt the cross-correlation formalism established for complex-valued harmonics to real-valued harmonics, as the latter are predominantly used in the field of Ambisonics ? Can we compute the correlation of spherical spectra of different bandwidths ? What is the impact of the finite sampling distribution used for integration on the $SO(3)$ space ? And most importantly, is the cross-correlation an efficient measure for the classification of 3D radiation patterns ?

1 Introduction

Spherical correlation is a tool that allows the evaluation of similarity between radiation data on the sphere based on its spherical harmonics expansion. This is well discussed in the mathematical literature and widely used for 3D shape-matching in the field of image processing. The state of the art is introduced in [17], building on the foundation of the spatial Fourier transform [5]. However, so far, the practical use of spherical correlation in the field of acoustics remains limited and challenging.

Guillon [6, 7] uses spherical correlation to compute similarities between spatial frequency response surfaces (SFRS), and later to clusterize a dataset of SFRS. This work is probably the most detailed usage of spherical correlation in spatial audio thus far. Moreau [20, 21] employs spatial correlation to assess qualitatively a directivity model of spherical microphone arrays against measured data. However, his work does not operate in the spherical harmonics domain and does not apply rotational matching. Similar to our study, Hohl and Zotter [10, 30] use the spherical correlation coefficient as a similarity measure of radiation patterns of musical instruments. They examine whether different partials at the same frequency, but originating from different played pitches, exhibit similar radiation on a given instrument. This is promising work, but their short paper does not provide much detail.

Our study is both motivated and facilitated by the availability of a large database of anechoic measurements of acoustic instrumental radiation data produced at the Technische Universität (TU) Berlin [28, 24]. With radiation patterns for 41 modern and historical orchestral instruments, the database suggests several questions : how do the radiation patterns of partials and registers of a given instrument correlate with each other, how do they correlate with those of different instruments, and how could these correlations be used to classify and navigate the database ?

2 Theoretical background

2.1 Cross-correlation on the sphere

Given two shapes f and g, how do we find the rotation to align them best ? Let f be a square-integrable function on the unit sphere $f \in L^2(\mathbb{S}^2)$. In the simple case, let us assume that g is a rotated version of f, i.e. $f = \Lambda_R(g)$ for some 3D rotation R. We denote Λ_R the rotational operator defined such that $\forall \boldsymbol{\Omega} \in \mathbb{S}^2$

$$\Lambda : L^2(\mathbb{S}^2) \to L^2(\mathbb{S}^2)$$
$$\Lambda_R(g)(\boldsymbol{\Omega}) = g\left(R^{-1}(\boldsymbol{\Omega})\right) . \tag{1}$$

We wish to find the rotation R. In the more general case, given the two patterns f and g, we wish to find the rotation that best aligns the two shapes on the sphere. This can be accomplished by evaluating the cross-correlation between the two functions

$$C_R(f, g) = \int_{\mathbb{S}^2} f(\boldsymbol{\Omega}) \, \overline{\Lambda_R(g)(\boldsymbol{\Omega})} \, d\boldsymbol{\Omega} , \tag{2}$$

and finding the rotation R that maximizes the above integral [17]. This has a number of useful applications, e.g. in the field of 3-D shape-matching, also known as shape registration [14, 15, 16, 8, 26, 25].

How do we maximize Equation 2 ? Evaluating $C_R(f, g)$ for all possible rotations in the spatial domain is a time-consuming task. Instead, we undertake it in the spatial Fourier domain. Since f and g are square-integrable on the sphere, we can write their Fourier expansions [5] :

$$f(\boldsymbol{\Omega}) = \sum_{n=0}^{N} \sum_{m=-n}^{m=+n} f_n^m \, Y_n^m(\boldsymbol{\Omega}) . \tag{3}$$

Here we have further assumed that f and g are bandlimited, with their bandwidth $B = (N + 1)$, N being the maximum order of the Fourier expansion. $Y_n^m(\boldsymbol{\Omega})$ are the spherical harmonic functions, and f_n^m are the Fourier coefficients of f. A well-known property of the (Euclidian) Fourier transform is that a translation in the time domain is interpreted as a phase shift in the frequency domain. For the Fourier transform

in $\mathbb{S}^2$, this property means that the magnitudes of the Fourier coefficients are invariant under rotation : writing $f_n(\mathbf{\Omega})$ for the nth frequency component of f

$$f_n(\mathbf{\Omega}) = \sum_{m=-n}^{m=+n} f_n^m \, Y_n^m(\mathbf{\Omega}) \,, \qquad (4)$$

the quantity $|f_n(\mathbf{\Omega})|$ is invariant under rotation.

Furthermore, the spherical harmonic basis functions of each order n transform among themselves under rotation according to

$$\Lambda_R(Y_n^m(\mathbf{\Omega})) = \sum_{m'=-n}^{m'=+n} Y_n^m(\mathbf{\Omega}) \, D_{mm'}^n(R) \,, \qquad (5)$$

where $D_{mm'}^n(R)$ is the Wigner-D function (see section 7).

Equation 5 is valid for complex-valued spherical harmonics. When considering real-valued spherical harmonics, a similar result holds, however involving the Wigner-d function instead of Wigner-D; details can be found for instance in [23] (Equations (16) to (20)).

Now, using relations 3, 4, and 5, it is possible to simplify 2 into :

$$C_R(f,g) = \sum_{n=0}^{N} \sum_{|m| \leq n} \sum_{|m'| \leq n} f_n^{-m} \overline{g_n^{m'}} (-1)^{m-m'} D_{mm'}^n(R) \,. \qquad (6)$$

A complete demonstration can be found for instance in [17]. Equation 6 allows us efficiently to compute the cross-correlation by combining the Fourier coefficients of f and g. From this, we can now search for which rotation R maximizes $\mathcal{C}_R(f,g)$.

In equations 5 and 6, the Fourier coefficients are rotated by means of the explicit formulae with the Wigner-D functions (or Wigner-d for real-valued harmonics) ; in our practical implementation, we rather use recurrence relations [13] as this appears to be computationally more efficient.

2.2 Normalized cross-correlation

The normalized cross-correlation [11, 26, 7, 11] is simply a variant of Equation 2 normalized by the energy of f and g, written

$$\mathcal{C}_R(f,g) = \frac{\int_{\mathbb{S}^2} f(\mathbf{\Omega}) \, \overline{\Lambda_R(g)(\mathbf{\Omega})} \, d\mathbf{\Omega}}{\sqrt{\int_{\mathbb{S}^2} |f(\mathbf{\Omega})|^2 \, d\mathbf{\Omega} \, \cdot \, \int_{\mathbb{S}^2} |g(\mathbf{\Omega})|^2 \, d\mathbf{\Omega}}} \,. \qquad (7)$$

The numerator of this expression has already been developed in Equation 6. The denominator can be easily calculated thanks to Parseval's identity : $\int_{\mathbb{S}^2} |f(\mathbf{\Omega})|^2 \, d\mathbf{\Omega} = \sum_{n=0}^{N} \sum_{m=-n}^{m=+n} |f_n^m|^2$.

3 Searching for the optimal rotation R

A rotation in $\mathbb{R}^3$ can be equivalently represented by : (a) a 3×3 rotation matrix, (b) a set of 3 Euler angles (or alternatively 3 Tait–Bryan angles), (c) a unit quaternion, also known as a versor, or (d) an axis–angle representation (i.e. a unit vector indicating the direction of an axis of rotation, and an angle describing the magnitude of the rotation about the axis). The different properties – such as compactness, numerical stability,

computational cost, singularity or gimbal lock, etc. – of these formalisms can be easily found in the literature [4], as well as conversion formulae from one representation to another.

We denote as $SO(3)$ the 3D rotation group, also known as the special orthogonal group. $SO(3)$ contains all rotations R about the origin of three-dimensional Euclidean space : $SO(3) = \left\{ R \in \mathbb{R}^3 \mid RR^T = I_3 \text{ and } \det(R) = +1 \right\}$, where I_3 is the 3×3 identity matrix. In other words, $SO(3)$ is the subgroup of orthogonal matrices with determinant $+1$.

We need to explore the $SO(3)$ space in order to determine $\underset{R \in SO(3)}{\arg\max} \; \mathcal{C}_R(f,g)$ that maximizes Equations 6 or 7. One possibility is to use a gradient descent technique. Gradient descent has been formalized on the $SO(3)$ rotation group in [27, 2]. The procedure requires approximation of the directional derivatives, with an adjustable small step size, in order to converge to the nearest local maximum. It might also be necessary to restart the algorithm from several initial values. Choosing the optimal step size or the initial value is not a trivial task. Therefore we have decided not to use a gradient descent, but instead to proceed with brute force sampling in $SO(3)$.

3.1 Sampling the rotation group $SO(3)$

The rotation group $SO(3)$ can be parameterized by quaternions, Euler angles, or orthogonal matrices. Sampling these different parameter spaces is not a trivial task, and they can generate sampling distributions of $SO(3)$ with various properties. To solve our problem, we typically need a uniform and deterministic sampling scheme. The definition of "uniform" is subject to interpretation, but essentially the sampling grid should ensure both global coverage and local separation. This problem has been studied for instance in [19, 29, 18]. An extensive analysis is beyond the scope of this article.

3.1.1 Parametrization by Euler angles

For the sake of simplicity, we will follow [17, 6] and use a regular sampling in terms of ZYZ Euler angles (α, β, γ) :

$$\alpha_j = \gamma_j = \frac{2\pi j}{2B} \text{ and } \beta_k = \frac{\pi(2k+1)}{4B} \,, \qquad (8)$$

with $0 \leq j, k < 2B$. According to [17], this sampling scheme is suitable for the analysis of bandlimited functions with bandwidth B. With this sampling, the size of the search space is $2B \times 2B \times 2B$.

Note that the "null" rotation ($\alpha = \beta = \gamma = 0$) is not part of the sampling grid. Consequently, correlating a signal with itself will not yield $\alpha = \beta = \gamma = 0$, but rather $\beta = \pi/(4B)$. This is counter-intuitive but not problematic. To circumvent this, it has been proposed [6] first to rotate one of the patterns, f or g, by $-\pi/(4B)$ around the $\mathbf{y}$ axis.

We should also note that the "true" rotation R might not be on the sampling grid. Therefore, we might only find an approximate solution $\hat{R}$ that should be close to R. The notion of "distance" in $SO(3)$ will be discussed in section 3.1.3.

3.1.2 Angle and axis representation

Any 3D rotation can be represented by an angle-axis representation. This formalism is useful for visualizing the projective space in $\mathbb{R}^3$ [29] : each rotation is drawn as a vector with direction $\mathbf{n}$ (the axis of the rotation) and a magnitude corresponding to ϑ (the rotation angle). As can be observed graphically in Figure 1, the Hopf fibration sampling proposed in [29] is highly uniform. Yet, for the remainder of this article, we will use the basic Euler sampling (Equation 8) for its simplicity and scalability (with respect to B).
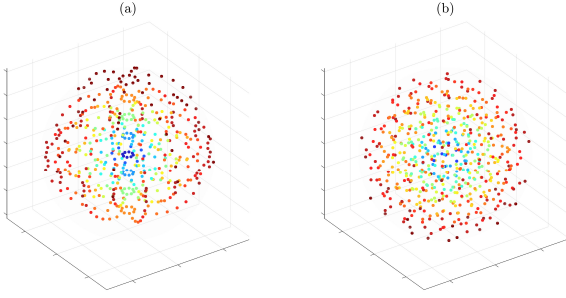

FIGURE 1 – Visualization of $SO(3)$ sampling grids using the angle-axis representation. (a) Regular sampling of Euler angles (as in Equation 8) with $B = 4$, leading to $(2B)^3 = 512$ elements ; (b) Uniform incremental sampling using the Hopf fibration [29] (with 576 sampling points). The color represents the magnitude of the rotation (from blue to red).

3.1.3 Distance measure of two rotation matrices

Various functions for measuring distance between 3D rotations have been proposed in the literature. The usual (angular) distance between two rotation matrices $R, Q \in SO(3)$ is given by [19, 9, 3] $\mathrm{d}_1(R, Q) = \mathrm{acos}\left(\frac{1}{2}\left(\mathrm{tr}\left(QR^T\right) - 1\right)\right)$. This metric measures the angle of rotation needed to map the transformation R to the transformation Q, or equivalently the angle of rotation associated to the transformation QR^{-1}. Alternatively, we can interpret $\mathrm{d}_1(R, Q)$ as a scaled Froebenius norm, since $\mathrm{d}_2(R, Q) = \|R - Q\|_{\mathrm{F}} = 2\sqrt{2}\sin\left(\frac{\mathrm{d}_1(R,Q)}{2}\right)$, where $\|\cdot\|_{\mathrm{F}}$ is the Frobenius norm defined as $\|R\|_{\mathrm{F}} = \sqrt{\mathrm{tr}\left(RR^T\right)}$. Huynh [12] presents a detailed analysis of various metrics, and demonstrates that many of them are functionally equivalent. Huynh concludes that the following metric, based on quaternions, is both spatially and computationally more efficient : $\mathrm{d}(R, Q) = 1 - |\mathbf{q_R} \cdot \mathbf{q_Q}|$, where $\mathbf{q_R}$ is the unit quaternion corresponding to matrix R, and $\cdot$ denotes the inner product. This metric will be used for the remainder of this article.

Note that, while a distance metric in $SO(3)$ is useful, it must be handled with care in the context of this paper : consider for example an axis-symmetric pattern f, for example a cardioid in the $\mathbf{y}$ direction. Rotate f around the $\mathbf{z}$-axis with $R_0 \equiv (\alpha_0, \beta_0, \gamma_0) = (\pi, 0, 0)$. Rotate f around the $\mathbf{x}$-axis with $R_1 \equiv (\alpha_1, \beta_1, \gamma_1) = (0, 0, \pi)$. Both scenarios result in the exact same pattern g ; however, the two rotations differ, and their distance is $\mathrm{d}(R_0, R_1) = 1$!

3.2 Numerical simulations

3.2.1 Impact of $SO(3)$ sampling

As discussed in the previous paragraphs, the choice of the sampling grid for $SO(3)$ might have an influence on the accuracy and efficiency of the maximization problem 7. For the sake of simplicity, we consider only the regular Euler sampling of equation 8. However, we investigate the use of "oversampling" i.e. we use a smaller step size in discretizing the Euler angles (α, β, γ). Instead of using $2B$ samples for each parameter, we use $\mathcal{N} \geq 2B$. This seems relevant as our scenario involves spatial functions with relatively low bandwidth ($B = 5$ if we consider the radiation patterns available in the TU Berlin database) compared to other authors (Kostelec [17] typically presents results with $B = 128$). With such low bandwidth, the angular step size is very large ($\pi/B = 36°$), and therefore high angular misalignment might occur. Of course, oversampling the search grid results in higher computation time, but that is not the focus of this paper.

We run the following numerical simulation : (a) generate a random spatial function f with a limited bandwidth B, (b) generate a random rotation matrix [1] R in $SO(3)$ and compute $g = \Lambda_R(f)$, (c) sample $SO(3)$ and search for the rotation matrix $\hat{R}$ that maximizes the cross-correlation, (d) compute the cross-correlation after rotational matching, i.e. the cross-correlation between g and $\Lambda_{\hat{R}}(f)$, (e) repeat the simulation for various samplings of $SO(3)$, varying the oversampling factor $\mathcal{N}/(2B)$, (f) repeat the simulation for various bandwidths B. For each test case, we perform 10000 Monte-Carlo runs. The results are presented in Figure 2. For each simulated bandwidth B, it can be observed that oversampling the search space improves accuracy, allowing for a higher cross-correlation (closer to 1), and a smaller distance (closer to 0) between the expected and estimated rotation matrices.
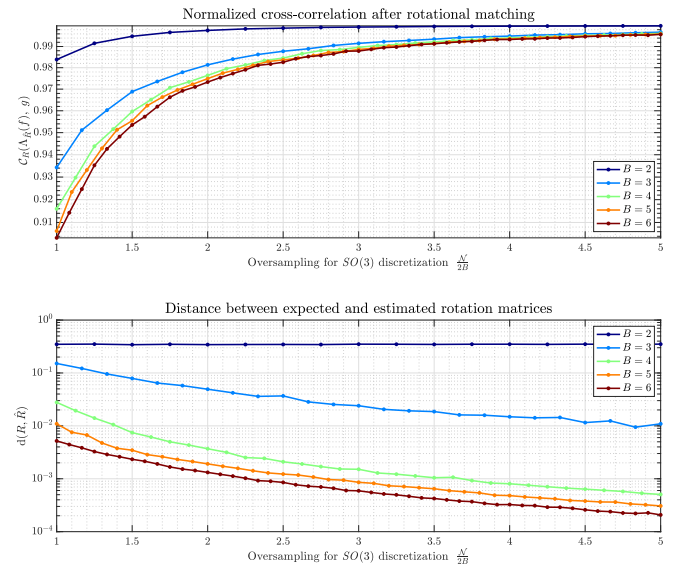

FIGURE 2 – Impact of oversampling the $SO(3)$ search space.

3.2.2 Comparing two patterns of different bandwidths

The cross-correlation function in equation 6 assumes that the two patterns f and g have the same bandwidth. In practice, it might be desirable also to compare patterns with different bandwidths.

We run the following numerical simulation : (a) generate a random spatial function f with a limited bandwidth $B_f = 11$, (b) generate a random rotation matrix R and compute $g = \Lambda_R(f)$, (c) reduce the bandwidth of g to $B_g \leq B_f$ by zeroing the higher order components, (d) compute the cross-correlation after rotational matching, i.e. the cross-correlation between g and $\Lambda_{\hat{R}}(f)$ (e) repeat the simulation for various truncation bandwidth B_g. For each test case, we perform 10000 Monte-Carlo runs. The results are presented in Figure 3. We observe that it is possible to compare two rotated cousins even if their bandwidths differ : when $B_f - B_g$ increases, the cross-correlation decreases, which is expected, but the patterns are correctly aligned since the distance between rotation matrices $\mathrm{d}(R, \hat{R})$ is low. When the mismatch between B_f and B_g becomes very large $(B_f - B_g) > 6$, the accuracy of the rotational matching decreases significantly.
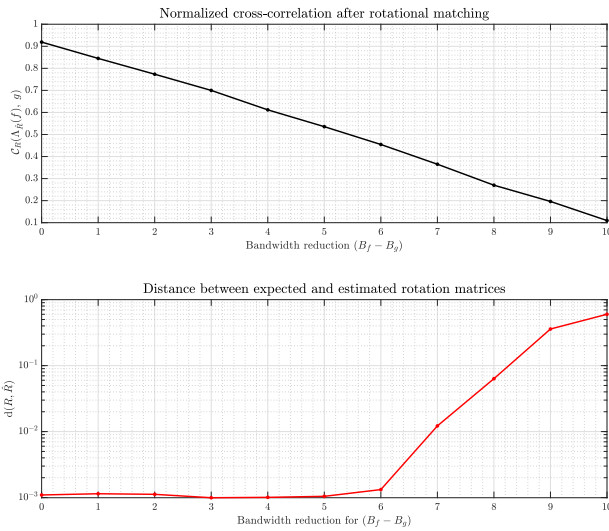

FIGURE 3 – Comparing two patterns of different bandwidths.

3.2.3 Comparing two arbitrary patterns

In the most general case, we are interested in comparing two arbitrary radiation patterns, not only rotated cousins. Such a scenario generally yields $|\mathcal{C}_{\hat{R}}(f, g)| < 1$, but the rotational alignment can still be effective. In Figure 4, we simulate two arbitrary patterns, having different bandwidth, shape, and orientation of their "main lobe". We observe that f is properly aligned with g. The resulting correlation coefficient is $\mathcal{C}_{\hat{R}}(f, g) \approx 0.45$.

4 Visualization with multidimensional scaling

With an approach to pairwise spherical correlation in place, we can now examine applications to classify and navigate
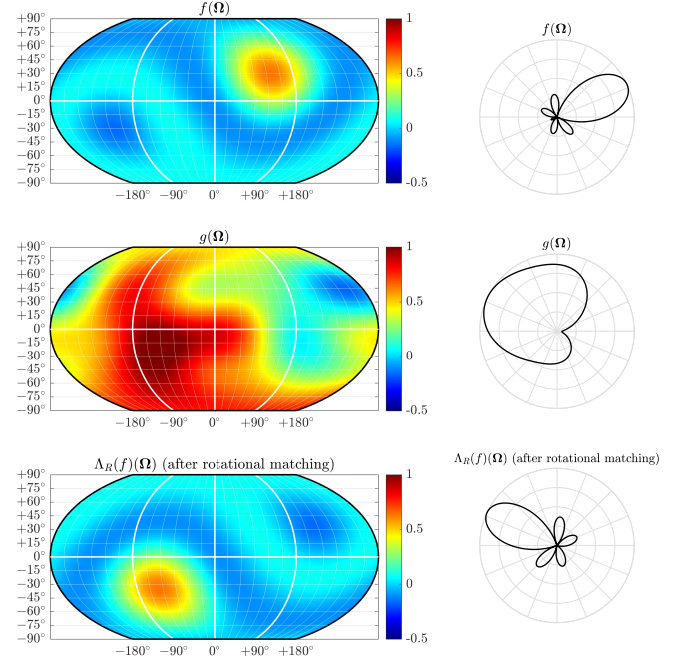

FIGURE 4 – Example of rotational matching. Left : visualization on the sphere. Right : restriction on the horizontal plane.

larger collections of 3D radiation patterns. One approach is to apply multidimensional scaling (MDS). MDS is used to translate information about the pairwise distances (or dissimilarities) among a set of n objects or individuals into a configuration of n points mapped into an abstract Cartesian space. MDS is therefore a means of visualizing the level of similarity of samples within a dataset.

We begin with a proof of concept using the functions $Y_n^m(\mathbf{\Omega})$ as our dataset. First we compute the normalized cross-correlation between all pairs $Y_{n_1}^{m_1}(\mathbf{\Omega})$ and $Y_{n_2}^{m_2}(\mathbf{\Omega})$. From this similarity matrix, we perform MDS and visualize the information map, choosing a dimensionality of 2 for simplicity of visualization and interpretation. The results in Figure 5
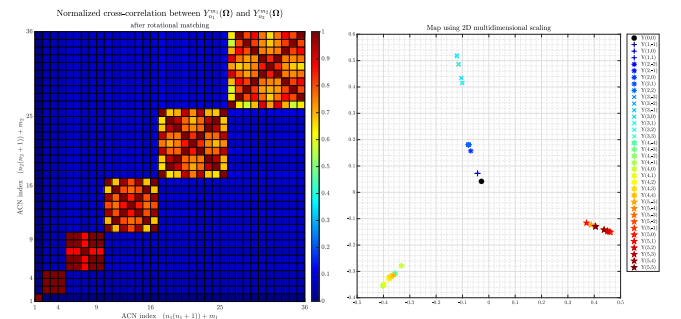

FIGURE 5 – Left : normalized cross-correlation between all pairs $Y_{n_1}^{m_1}(\mathbf{\Omega})$ and $Y_{n_2}^{m_2}(\mathbf{\Omega})$. Right : resulting 2D MDS.

for maximum order $N = 5$ show that, within each order, the functions are highly correlated. For order $N = 1$, the three

functions are even fully correlated, which is expected as these spherical harmonics are dipoles along the $\mathbf{x}$, $\mathbf{y}$, and $\mathbf{z}$ axes (i.e. they are exactly rotated cousins). The map clearly exhibits six clusters of samples, each cluster corresponding to a given order N. Orders 0, 1, and 2 are relatively close, while 3, 4 and 5 are maximally distant from the lower orders and from each other.

5 Application to measured data

We now apply the approaches presented in the previous sections to measured radiation patterns of musical instruments. Our source is the acoustic instrumental radiation database, containing 41 modern and historical orchestral instruments, made available by the TU Berlin [28, 24].

5.1 Radiation patterns of partials

To test the claim in [10] that instrumental partials with the same frequency have correlated radiation patterns, we compute a similarity matrix containing the pairwise correlation between partials of different played pitches. The matrix is organized in blocks each containing a chromatic scale, with each successive block representing a different partial for each played note. With this matrix arrangement, partials with matching frequency are located on the secondary diagonals. Figure 6 illustrates examples of results for clarinet and cello. It can be observed that different partials at the same frequency exhibit strongly correlated radiation, regardless of the played pitch from which they originate. Other findings are also in line with [10], however the results are less obvious. This might be partly explained by the lower resolution of TU Berlin database, leading to a lower bound for the spatial aliasing frequency.
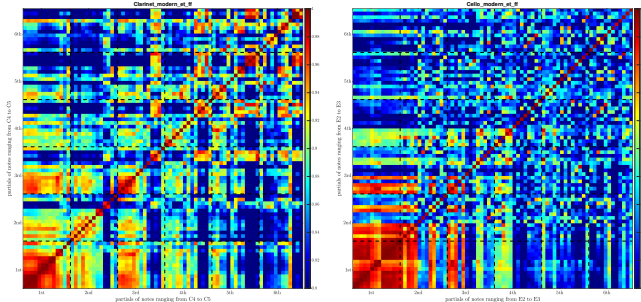

FIGURE 6 – First 6 partials of the clarinet in B-flat for pitches ranging from $C4$ to $C5$ (left) and of the cello for pitches ranging from $E2$ to $E3$ (right).

5.2 MDS applied to TU Berlin data

Another motivation for this work is to classify the TU Berlin database for subsequent manipulation with corpus-based synthesis techniques : by organizing instrumental samples according to their spatial characteristics, the resulting low-dimensional representation can be used, along with other audio descriptors, to navigate the sample corpus. We applied MDS analysis as presented in section 4 to measured radiation patterns of different instruments for various played pitches. An example is presented in Figure 7. The color code

corresponds to the three categories of instruments proposed by Shabtai [24]. In red : instruments with one expected radiation point ; this mainly includes the brass instruments. In blue : instruments with several expected radiation points, such as woodwind instruments, with sound radiated by the bell, the fingering holes, and the mouthpiece. In black : instruments with a full body radiating sound, such as string instruments. We observe that MDS based on spherical correlation allows us efficiently to segregate and organize the instruments, in accordance with their expected category.
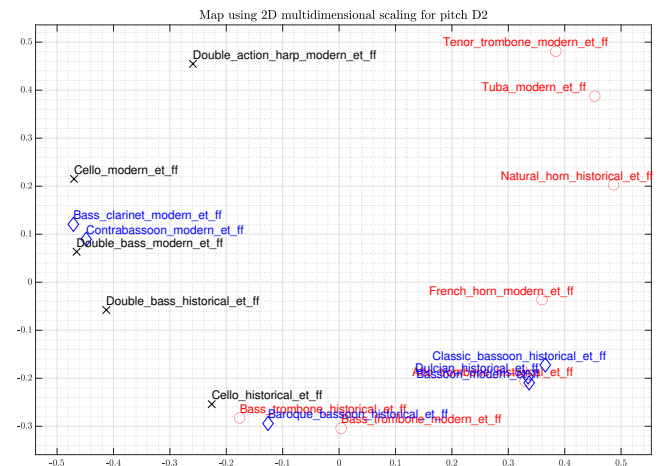

FIGURE 7 – MDS applied to radiation patterns of the pitch $D2$ for various brass, woodwind, and string instruments.

6 Conclusion

In this paper, we discussed the use of cross-correlation on the sphere as a similarity measure for the classification of 3D radiation patterns. We showed that this tool can facilitate thorough analysis of directivity pattern similarities across partials of one instrument or between different instruments. However, spherical correlation can only capture rotational resemblance ; it might therefore be necessary also to consider energetic criteria when comparing radiation patterns. Future work will investigate other spatial descriptors for the classification of the 3D database of orchestral instruments. A further direction will be transformations of radiation patterns based on interpolation between correlated and rotated pairs, which we hypothesize will give more consistent results than interpolation between unrotated patterns, to be applied in the context of regression for a machine learning algorithm.

Références

[1] J. Arvo. Random Rotation Matrices. In J. Arvo, editor, *Graphics Gems II*, pages 355 – 356. Morgan Kaufmann, San Diego, 1991.

[2] G. S. Chirikjian, P. T. Kim, J.-Y. Koo, and C. H. Lee. Rotational matching problems. *International Journal of Computational Intelligence and Applications*, 4(4) :401 – 416, 2004.

[3] D. Deboy and F. Zotter. Acoustic center and orientation analysis of sound-radiation recorded with a surrounding spherical microphone array. In *Proc. of the 2nd International Symposium on Ambisonics and Spherical Acoustics*, Paris, May 2010.

[4] J. Diebel. Representing Attitude : Euler Angles, Unit Quaternions, and Rotation Vectors. Technical report, Stanford University, 2006.

[5] J. Driscoll and D. Healy. Computing Fourier Transforms and Convolutions on the 2-Sphere. *Advances in Applied Mathematics*, 15(2) :202 – 250, 1994.

[6] P. Guillon. *Individualisation des indices spectraux pour la synthèse binaurale : recherche et exploitation des similarités inter-individuelles pour l'adaptation ou la reconstruction de HRTF*. PhD thesis, Université du Maine, 2009.

[7] P. Guillon and R. Nicol. Head-Related Transfer Function reconstruction from sparse measurements considering a priori knowledge from database analysis : a pattern recognition approach. In *Proc. of the 125th Convention of the Audio Engineering Society*, San Francisco, October 2008.

[8] B. Gutman, Y. Wang, T. Chan, P. M. Thompson, and A. W. Toga. Shape Registration with Spherical Cross Correlation. In X. Pennec, editor, *Proc. of the 2nd Workshop on Mathematical Foundations of Computational Anatomy (MICCAI)*, pages 56 – 67, New York, 2008.

[9] R. Hielscher, J. Prestin, and A. Vollrath. Fast Summation of Functions on the Rotation Group. *Mathematical Geosciences*, 42 :773 – 794, October 2010.

[10] F. Hohl and F. Zotter. Similarity of musical instrument radiation-patterns in pitch and partial. In *Proc. of the Fortschritte der Akustik, DAGA*, Berlin, March 2010.

[11] B. Huhle, T. Schairer, and W. Straßer. Normalized Cross-Correlation using SOFT. In *Proc. Int. Workshop on Local and Non-Local Approximation in Image Processing*, pages 82 – 86, 2019.

[12] D. Q. Huynh. Metrics for 3D Rotations : Comparison and Analysis. *J. Math. Imaging Vis.*, 35(2) :155 – 164, oct 2009.

[13] J. Ivanic and K. Ruedenberg. Rotation Matrices for Real Spherical Harmonics. Direct Determination by Recursion. *J. Phys. Chem.*, 100 :6342 – 6347, 1996.

[14] M. Kazhdan and T. Funkhouser. Harmonic 3D Shape Matching. In *Proc. of the ACM SIGGRAPH Conference Abstracts and Applications*, page 191, New York, 2002.

[15] M. Kazhdan, T. Funkhouser, and S. Rusinkiewicz. Rotation Invariant Spherical Harmonic Representation of 3D Shape Descriptors. In *Proc. of the Eurographics Symposium on Geometry Processing*, pages 167 – 175, June 2003.

[16] M. Kazhdan, T. Funkhouser, and S. Rusinkiewicz. Symmetry Descriptors and 3D Shape Matching. In *Proc. of the Eurographics/ACM SIGGRAPH Symposium on Geometry Processing*, pages 115–123, New York, 2004.

[17] P. J. Kostelec and D. N. Rockmore. FFTs on the Rotation Group. *Journal Fourier Anal Appl*, 14 :145 – 179, 2008.

[18] J. Kuffner. Effective sampling and distance metrics for 3D rigid body path planning. In *Proc. IEEE International Conference on Robotics and Automation (ICRA)*, volume 4, pages 3993 – 3998, 2004.

[19] J. C. Mitchell. Sampling Rotation Groups by Successive Orthogonal Images. *SIAM Journal on Scientific Computing*, 30(1) :525 – 547, 2008.

[20] S. Moreau. *Étude et réalisation d'outils avancés d'encodage spatial pour la technique de spatialisation sonore Higher Order Ambisonics : microphone 3D et contrôle de distance*. PhD thesis, Université du Maine, 2006.

[21] S. Moreau, J. Daniel, and S. Bertet. 3D Sound Field Recording with Higher Order Ambisonics – Objective Measurements and Validation of Spherical Microphone. In *Proc. of the 120th Convention of the Audio Engineering Society*, Paris, 2006.

[22] T. Risbo. Fourier transform summation of Legendre series and D-functions. *Journal of Geodesy*, 70(7) :383–396, July 1996.

[23] D. W. Ritchie and G. J. L. Kemp. Fast Computation, Rotation, and Comparison of Low Resolution Spherical Harmonic Molecular Surfaces. *Journal of Computational Chemistry*, 20(4) :383 – 395, 1999.

[24] N. R. Shabtai, G. Behler, M. Vorländer, and S. Weinzierl. Generation and analysis of an acoustic radiation pattern database for forty-one musical instruments. *Journal of the Acoustical Society of America*, 141(2) :1246 – 1256, 2017.

[25] L. Shen, H. Huang, F. Makedon, and A. J. Saykin. Efficient Registration of 3D SPHARM Surfaces. In *Proc. of the 4th Canadian Conference on Computer and Robot Vision*, pages 81 – 88, Montreal, May 2007.

[26] L. Sorgi and K. Daniilidis. Normalized Cross-Correlation for Spherical Images. In T. Pajdla and J. Matas, editors, *Computer Vision - ECCV 2004*, pages 542 –5 53, Berlin, 2004. Springer.

[27] D. Stein, E. R. Scheinerman, and G. S. Chirikjian. Mathematical Models of Binary Spherical-Motion Encoders. *IEEE Transactions on Mechatronics*, 8(2) :234 – 244, 2003.

[28] S. Weinzierl, M. Vorländer, G. Behler, F. Brinkmann, H. von Coler, E. Detzner, J. Krämer, A. Lindau, M. Pollow, F. Schulz, and N. R. Shabtai. A Database of Anechoic Microphone Array Measurements of Musical Instruments - Recordings, Directivities, and Audio Features. Technical report, TU Berlin, 2017.

[29] A. Yershova, S. Jain, S. M. LaValle, and J. C. Mitchell. Generating Uniform Incremental Grids on SO(3) Using the Hopf Fibration. *The International Journal of Robotics Research*, 29(7) :801–812, 2010.

[30] F. Zotter. *Analysis and Synthesis of Sound-Radiation with Spherical Arrays*. PhD thesis, IEM, Graz, 2009.

7 Annex : Wigner-D function

Considering Euler angles with the ZYZ convention, the rotation matrix R can be expressed as a rotation of α about the $\mathbf{z}$ axis, followed by a rotation β about the $\mathbf{y}$ axis, and finally a rotation γ about the $\mathbf{z}$ axis : $R_{zyz}(\alpha, \beta, \gamma) = R_z(\alpha) \, R_y(\beta) \, R_z(\gamma)$ with :

$$R_z(\alpha) = \begin{pmatrix} \cos\alpha & -\sin\alpha & 0 \\ \sin\alpha & \cos\alpha & 0 \\ 0 & 0 & 1 \end{pmatrix} \; R_y(\beta) = \begin{pmatrix} \cos\beta & 0 & \sin\beta \\ 0 & 1 & 0 \\ -\sin\beta & 0 & \cos\beta \end{pmatrix}$$

and $0 \leq \alpha, \gamma < 2\pi$ and $0 \leq \beta \leq \pi$. With this convention, the Wigner-D function $D^n_{mm'}(R)$, required to rotate complex-valued spherical harmonics, is written

$$D^n_{mm'}(\alpha, \beta, \gamma) = e^{-im\alpha} \, d^n_{mm'}(\beta) \, e^{-im'\gamma} , \qquad (9)$$

where $d^n_{mm'}(\beta)$ is the Wigner-d function [22].